International Journal of Heat and Mass Transfer 158 (2020) 119999

Contents lists available at ScienceDirect

International Journal of Heat and Mass Transfer

journal homepage: www.elsevier.com/locate/hmt

The effect of gas-phase transport on Marangoni convection in volatile binary fluids driven by a horizontal temperature gradient

Tongran Qin[a,*], Roman O. Grigoriev[b]

[a] The Wallace H. Coulter Department of Biomedical Engineering, Georgia Institute of Technology, Atlanta, GA 30332, USA
[b] School of Physics, Georgia Institute of Technology, Atlanta, GA 30332, USA

ARTICLE INFO

Article history:
Received 1 January 2020
Revised 11 May 2020
Accepted 25 May 2020
Available online 30 June 2020

Keywords:
Marangoni convection
Buoyancy-Marangoni convection
Free-surface flows
Two-phase flows
Phase change
Binary fluids
Surface tension effects
Thermocapillarity
Solutocapillarity
Heat pipes

ABSTRACT

Recent experimental and numerical studies of convection in confined layers of volatile binary liquids with a free surface subjected to a horizontal temperature gradient have observed a reversal in the direction of interfacial flow as the concentration of air in the vapor space above the liquid is decreased. These observations suggest that transport in the gas phase has a significant effect on the balance between thermocapillary and solutocapillary stresses, the competition between which determines the flow direction. In order to develop a quantitative description of the flow reversal, we use the two-sided (liquid/gas) transport model introduced previously to obtain approximate analytical solutions for the interfacial temperature and composition of the liquid, hence predict thermocapillary and solutocapillary stresses, and the flow direction. Therefore, our solutions provide useful guidelines for choosing the optimal binary coolants composition and operating conditions for thermal management applications. Despite the complex nature of this problem, we have found that the mass transport in the gas phase is effectively one-dimensional and independent of the flow in moderate to large aspect-ratio cavity for sufficiently low temperature gradients, which allows this problem to be simplified and solved analytically in a sequential manner. Our theoretical predictions agree well with the results of numerical simulations, which indicates that the analytical analysis captures the essential physics of the problem.

1. Introduction

It is well-known that surface tension effects play a dominant role in microscale fluid flows in terrestrial conditions and even at macroscopic scales in microgravity. In particular, thermocapillary stresses arise at the free surface of nonisothermal fluids due to surface tension variation with temperature. For most simple fluids, thermocapillary stresses cause the flow in the direction opposite to the thermal gradient as surface tension decreases with increasing temperature. In some practical applications, such as in thermal management devices that rely on phase change, thermocapillarity plays an adverse role, pulling the liquid away from the hot region and promoting dry-out.

Dry-out can be reduced or eliminated using self-rewetting binary fluids [1] (mainly dilute aqueous solutions of long-chain alcohols) characterized by surface tension which increases with temperature [2]. Indeed, recent experimental investigations have shown that thermal performance of evaporative cooling devices could be significantly improved using self-rewetting fluids, under both terrestrial [3–6] and microgravity conditions [7–9]. The self-rewetting effect, however, is only limited in certain binary fluids within a range of temperatures [10], and the direction of the flow can be reversed over a much wider range of temperatures by using binary fluids with the more volatile component having a lower surface tension (e.g., aqueous solutions of short-chain alcohols). For such fluids, solutocapillary stresses which arise due to surface tension variation with liquid composition oppose thermocapillary stresses [11–14], and flow reversal is observed when solutocapillary stresses dominate [15].

While thermocapillary stresses arise for any fluids, simple or binary, volatile or nonvolatile, solutocapillary stresses of comparable magnitude can only arise mostly in volatile binary liquids, where differential phase change leads to concentration variation at the free surface. The strength of solutocapillary stresses depends on both the variation of surface tension with concentration and the concentration gradient along the free surface. The former is related to the mean composition of the liquid, while the latter is determined by differential phase change, which is strongly affected by the presence of noncondensable gases (such as air), which are well known to suppress phase change [16]. Recent experimental [15] and numerical [17,18] studies have investigated the dependence of the flow in a layer of methanol-water mixture on the

* Corresponding author.
E-mail address: tongran@gatech.edu (T. Qin).

https://doi.org/10.1016/j.ijheatmasstransfer.2020.119999
0017-9310/

composition of the two phases characterized by the mean concentration (molar fraction) of methanol $\bar{Y}_m$ in the liquid and the mean concentration of air $\bar{X}_a$ in the gas. It was determined that the flow is most sensitive to the composition of the gas phase: flow reversal requires $\bar{X}_a$ to be very low (a few percent or less). The dependence on the composition of the liquid phase was found to be much weaker, with the solutocapillary effect being somewhat stronger at low values of $\bar{Y}_m$.

The resolution of those two studies, however, was too low to determine the optimal values of $\bar{X}_a$ and $\bar{Y}_m$ which would generate the strongest flow in the direction of the applied temperature gradient. More importantly, while there are significant numerical and theoretical studies on Marangoni-driven flows in volatile binary fluids [17,19–24], we still lack the intuition about the interplay between transport of heat and mass across the liquid-vapor interface and in the bulk of the two layers, which controls the relative strength of thermo- and solutocapillary stresses. The main reason is that the transport equations for the momentum, heat, and mass are nonlinear and couple the flow, temperature, and concentration fields in the two layers, making this problem extremely complicated.

Our recent investigations of a similar problem involving a volatile *simple* fluid, on the other hand, came to an interesting and unexpected conclusion. Numerical simulations [25] showed that mass transport in the gas phase is effectively one-dimensional and independent of the flow field even for relatively high mass Péclet numbers. This result allowed decoupling the transport equations in the gas phase, leading to a dramatic simplification of the problem and allowing substantial analytical progress [26]. In particular, it became possible to compute the interfacial temperature and hence the Marangoni (thermocapillary) stresses that drive the flow. Our recent numerical simulations [17] for volatile *binary* fluids in the same geometry revealed that, while the gas phase becomes a ternary mixture, mass transport remains essentially one-dimensional, which suggests that the analytical approach could be extended to binary fluids. This paper shows that it is indeed possible to obtain approximate analytical solutions of the comprehensive two-sided transport model introduced in Ref. [17] yielding both the thermocapillary and solutocapillary stresses. The outline of the present study is as follows. We describe the transport model in Section 2. Its analysis as well as the comparison of the analytical predictions with the numerical results are presented Section 3. Section 4 contains the summary and conclusions.

2. Mathematical model

2.1. Governing equations

We will consider a flow in a layer of volatile binary liquid (water-methanol mixture) with a free surface confined along with its vapor and air in a rectangular test cell (cf. Fig. 1). The flow is driven by a horizontal temperature gradient in the extended (x) direction created by imposing a temperature difference $\Delta T = T_h - T_c$ between the outer surfaces of the two end walls. Previous experimental and numerical studies of surface-tension-driven flows in this geometry [27–29] showed that the liquid-vapor interface has a low curvature and the flow is nearly two-dimensional. Hence we will simplify the problem by considering the liquid layer to have a uniform thickness and the flow to be strictly two-dimensional and confined to the $x - z$ plane. The former assumption is justified when the dimensions L and W are much larger than the capillary length and the latter when the thickness of the layer is small compared to W.

The two-sided transport model [17] used for numerical simulations is reproduced here in a slightly condensed form to make the discussion self-contained. The flow in both phases is assumed

Fig. 1. The sketch of a test cell containing the liquid and air/vapor mixture. Gravity is pointing in the negative z direction. The inner dimensions are $H = W = 10$ mm, $L = 48.5$ mm, the walls are 1.25 mm thick, and the liquid (gas) layer has a thickness $d_l = 2.5$ mm ($d_g = 7.5$ mm).

incompressible

$$\nabla \cdot \mathbf{u} = 0, \tag{1}$$

and the momentum transport in the bulk is described by the Navier-Stokes equation

$$\rho(\partial_t \mathbf{u} + \mathbf{u} \cdot \nabla \mathbf{u}) = -\nabla p + \mu \nabla^2 \mathbf{u} + \rho \mathbf{g}, \tag{2}$$

where $\mathbf{u}$ is the velocity, p is the pressure, ρ and μ are the density and dynamic viscosity of the fluid, respectively, and $\mathbf{g} = -g\hat{\mathbf{z}}$ is the gravitational acceleration. Heat transport in the bulk is described by the advection-diffusion equation

$$\partial_t T + \mathbf{u} \cdot \nabla T = \alpha \nabla^2 T, \tag{3}$$

where T is the temperature and $\alpha = k/\rho C_p$ is the thermal diffusivity of the fluid.

The density of the liquid mixture is assumed to be

$$\rho_l = \rho_{l,m} + \rho_{l,w}, \tag{4}$$

where $\rho_{l,b}$ is the density of component b. Here and below the subscript denotes the phase (l for the liquid, g for the gas), and/or the component of the mixture (m for methanol, w for water, a for air). We will use the subscript i to denote the values at the liquid-gas interface. A linear dependence of the density of each component on the temperature is assumed,

$$\rho_{l,b} = \rho^0_{l,b}[1 - \beta_{l,b}(T - T_0)], \tag{5}$$

where $\beta_{l,b} = -\rho^{-1}_{l,b}\partial\rho_{l,b}/\partial T$ is the coefficient of thermal expansion and $\rho^0_{l,b}$ is the density of component b in the mixture at the reference temperature T_0 (here and below we will assume $T_0 = (T_c + T_h)/2$). We also have

$$\rho^0_{l,b} = n_l Y_b m^1_b, \tag{6}$$

where n_l is the total number density in the liquid, m^1_b is the mass of one molecule, and $Y_b = n_{l,b}/n_l$ is the concentration (molar fraction) of component b in the liquid phase.

The density and pressure of the gas mixture are

$$\begin{aligned} \rho_g &= \rho_{g,m} + \rho_{g,w} + \rho_{g,a}, \\ p_g &= p_{g,m} + p_{g,w} + p_{g,a}, \end{aligned} \tag{7}$$

where all components are assumed to be ideal,

$$\begin{aligned} \rho_{g,b} &= \frac{X_b p_g}{R_b T}, \\ p_{g,b} &= X_b p_g, \end{aligned} \tag{8}$$

$X_b = n_{g,b}/n_g$ is the concentration (molar fraction), n_g is the total number density in the gas, $R_b = R/M_b$ is the specific gas constant, and $M_b = m^1_b N_A$ is the molar mass of component b of the gas phase. We use the Boussinesq approximation, according to which

the spatial average of ρ_l and ρ_g is used on the left-hand-side (but not the right-hand-side) of the Navier-Stokes Eq. (2) for the liquid and the gas phase. Furthermore, we treat n_l and

$$n_g = \frac{p_g}{k_B T_0} \tag{9}$$

as spatially constant, which is justified along with the Boussinesq approximation for $\Delta T \ll T_0$. The pressure p_g is spatially nearly constant and is computed based on the incompressibility condition and mass conservation of the three components (air, water, methanol) [17].

With the assumptions of incompressible flow and constant total number density of the mixture, mass transport in the binary liquid mixture is described by the advection-diffusion equation for, say, water concentration

$$\partial_t Y_w + \mathbf{u}\cdot\nabla Y_w = \nabla\cdot(D_l \nabla Y_w), \tag{10}$$

where D_l is the binary mass diffusivity, and the methanol concentration is recovered from

$$Y_m = 1 - Y_w. \tag{11}$$

Here and below the subscript denotes the phase (l for the liquid, g for the gas), and/or the component of the mixture (m for methanol, w for water, a for air). We will use the subscript i to denote the values at the liquid-gas interface. Similarly, in the ternary gas phase, mass transport is described using a pair of equations

$$\partial_t X_b + \mathbf{u}\cdot\nabla X_b = \nabla\cdot(\mathfrak{D}_b \nabla X_b), \tag{12}$$

for water and methanol, where $\mathfrak{D}_b$ are the effective mass diffusivities [30], which are assumed to depend only on the average concentrations [17]. The concentration of air is hence given by

$$X_a = 1 - X_m - X_w. \tag{13}$$

Together, (12) and (13) describe mass transport in the ternary gas phase with arbitrary composition.

2.2. Boundary conditions

The system of coupled evolution Eqs. (1)–(3) and (10) for the liquid phase (or (12) for the gas phase) has to be solved in a self-consistent manner, subject to the boundary conditions describing the balance of momentum, heat, and number fluxes at the liquid-gas interface and at the inner surface of the walls of the cavity.

For simple fluids, over a wide range of conditions, phase equilibrium can be described by the Antoine equation

$$\ln p_b = A_b - \frac{B_b}{C_b + T}, \tag{14}$$

where p_b is the vapor pressure, and A_b, B_b, C_b are empirical coefficients. In developing a simplified description of the problem, it will be more convenient to instead use the Clausius-Clapeyron relation

$$\ln\frac{p_b}{p_b^0} = -\frac{\mathcal{L}_b}{R_b}\left(\frac{1}{T} - \frac{1}{T_0}\right), \tag{15}$$

where p_b^0 is the reference value of the vapor pressure at the reference temperature T_0. The two relations are equivalent for small deviations of T from T_0, provided the latent heat is defined according to

$$\mathcal{L}_b = \frac{B_b R_b T_0^2}{(C_b + T_0)^2}. \tag{16}$$

This can be easily verified by evaluating the expressions (14) and (15) and their derivatives with respect to T at T_0. For binary fluids, phase equilibrium is determined by an extended Raoult's law

$$p_{g,b} = \gamma_b p_b Y_b, \tag{17}$$

where γ_b is the activity coefficient of component b, which accounts for deviations from an ideal liquid mixture, $p_{g,b}$ is the corresponding partial pressure of the vapor, and p_b satisfies (14) (or (15)). In the following, we will use (17) in combination with (14) in the numerics, or in combination with (15) in the theoretical analysis, to define the saturation temperatures $T_{s,b}$ given the partial vapor pressures $p_{g,b}$. Note that $T_{s,b}$ does not correspond to the saturation temperature of a pure component b and depends on both X_b through (8) and Y_b through (17).

Phase change occurs locally where the thermodynamic free energy is different between the phases. The driving forces for mixtures include the temperature difference, pressure difference, and concentration difference across the interface [31]. The latter two effects are negligible in this study. Therefore, the number density flux describing phase change for each component of the volatile fluid can be described using the kinetic theory expression [32], which only includes the temperature difference

$$j_{i,b} = \frac{2\chi_b}{2-\chi_b}\frac{T_b}{T_i}\frac{T_i - T_{s,b}}{T_{s,b}} n_g X_b u_{t,b}, \tag{18}$$

where $T_b = \mathcal{L}_b/R_b$, χ_b is the accommodation coefficient, and

$$u_{t,b} = \sqrt{\frac{R_b T_i}{2\pi}} \tag{19}$$

is the characteristic thermal velocity. The corresponding mass flux is $J_{i,b} = m_b^1 j_{i,b}$.

Since air is noncondensable, we can write the mass/number flux balance on the gas side of the interface as

$$\begin{aligned} j_{i,b} &= n_g X_b \hat{\mathbf{z}}\cdot\mathbf{u}_g - n_g \mathfrak{D}_b\,\partial_z X_b, \\ j_{i,a} &= 0, \end{aligned} \tag{20}$$

while on the liquid side

$$j_{i,b} = n_l Y_b \hat{\mathbf{z}}\cdot\mathbf{u}_l - n_l D_l\,\partial_z Y_b. \tag{21}$$

The heat flux balance requires

$$\mathcal{L}_m m_m^1 j_{i,m} + \mathcal{L}_w m_w^1 j_{i,w} = k_g \partial_z T_g - k_l \partial_z T_l \tag{22}$$

and the temperature is assumed continuous

$$T_l = T_i = T_g. \tag{23}$$

The tangential components of the velocity across the interface are also continuous

$$(\mathbb{I} - \hat{\mathbf{z}}\hat{\mathbf{z}})\cdot(\mathbf{u}_l - \mathbf{u}_g) = 0, \tag{24}$$

while the normal components are related by mass flux balance

$$n_l \hat{\mathbf{z}}\cdot\mathbf{u}_l = n_g \hat{\mathbf{z}}\cdot\mathbf{u}_g = j_{i,m} + j_{i,w}. \tag{25}$$

Assuming flat interface and negligible effect of vapor recoil, the stress balance at the interface

$$\hat{\mathbf{x}}\cdot(\boldsymbol{\Sigma}_l - \boldsymbol{\Sigma}_g)\cdot\hat{\mathbf{z}} = \partial_x\sigma, \tag{26}$$

incorporates viscous drag between the two phases and the Marangoni (thermo- and solutocapillary) stresses, where σ is the surface tension and

$$\boldsymbol{\Sigma} = \mu\left[\nabla\mathbf{u} + (\nabla\mathbf{u})^T\right] - p\mathbb{I} \tag{27}$$

is the stress tensor. The surface tension of the methanol-water liquid mixture is described by a relation [33]

$$\sigma = f(Y_m)\sigma_m + [1 - f(Y_m)]\sigma_w \tag{28}$$

based on the fits to experimental data, where

$$f(Y_m) = Y_m\frac{1 + c_1(1 - Y_m)}{1 - c_2(1 - Y_m)}, \tag{29}$$

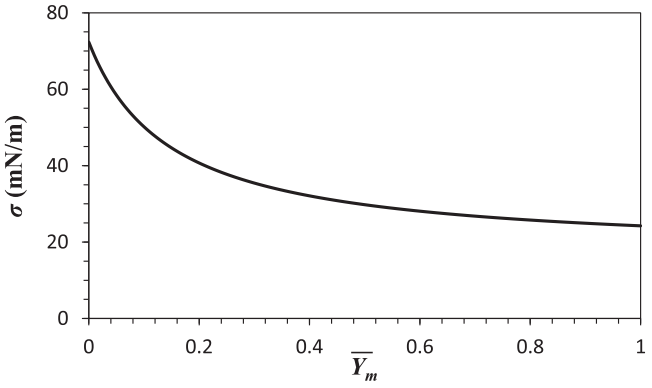

Fig. 2. Surface tension of methanol-water mixture as a function of the methanol concentration computed using (28).

with empirical parameters c_1 and c_2 (cf. Fig. 2). The surface tension of each component is assumed to be linear with respect to the temperature of the interface

$$\sigma_b = \sigma_b^0 + \sigma_b'(T_i - T_0), \tag{30}$$

where σ_b^0 is the surface tension of the pure substance at the reference temperature T_0 and $\sigma_b' = \partial\sigma_b/\partial T$ is the temperature coefficient of surface tension. With the help of relations (28)–(30), the right-hand-side of (26) can be rewritten as

$$\begin{aligned}\partial_x\sigma &= f'(Y_m)(\sigma_m - \sigma_w)\partial_x Y_m \\ &\quad + \left[f(Y_m)\sigma_m' + [1 - f(Y_m)]\sigma_w'\right]\partial_x T_i,\end{aligned} \tag{31}$$

where the first and the second term represent the soluto- and thermocapillary stresses, respectively.

Since the walls of the test cell are thin, one-dimensional conduction inside these is assumed, yielding the following mixed boundary conditions on the inside of the end walls:

$$\begin{aligned}T|_{x=0} &= T_c + k_\iota \frac{h_s}{k_s}\partial_x T, \\ T|_{x=L} &= T_h + k_\iota \frac{h_s}{k_s}\partial_x T,\end{aligned} \tag{32}$$

where $\iota = g$ ($\iota = l$) above (below) the contact line, h_s is the thickness and k_s is the conductivity of the walls. In typical experiments, the side walls are in contact with air, which is a poor conductor, so heat flux through the top and bottom walls can be ignored

$$\partial_z T = 0. \tag{33}$$

Standard no-slip boundary conditions $\mathbf{u} = 0$ for the velocity and no-flux boundary conditions for the concentrations

$$\begin{aligned}\partial_n X_b &= 0, \\ \partial_n Y_b &= 0\end{aligned} \tag{34}$$

are imposed on all the walls, where $\partial_n = \hat{\mathbf{n}}\cdot\nabla$, and $\hat{\mathbf{n}}$ is the unit vector normal to the wall. Additional details of the mathematical model and its numerical implementation as well as the relevant material parameters can be found in Ref. [17].

3. Results

Although the transport equations for the momentum, heat, and mass (1)–(13) show that the flow, temperature, and concentration fields are all coupled via advection, buoyancy, or various boundary conditions, as confirmed by our numerical simulations [17] and the analysis presented next, even in a moderate-aspect-ratio cavity, the mass transport in the gas phase is effectively one-dimensional and independent of the flow field for sufficiently low ΔT. Therefore, we follow an approach similar to that of Ref. [26] to obtain a simplified description of this problem. The simplified description relies on the governing equations listed in the previous section, with certain reasonable assumptions that allow some variables to be decoupled, and hence the problem to be solved sequentially.

First, the concentration fields X_m and X_w in the gas phase can be found based on mass transport in the gas phase. Then both the interfacial temperature T_i and the interfacial composition Y_m can be obtained with the help of phase equilibrium relations. These interfacial profiles determine the thermo- and solutocapillary stresses and hence the flow in the liquid layer. In particular, the direction of the flow along the interface can be determined by comparing the strength of the thermocapillary stresses and the (opposing) solutocapillary stresses. (While buoyancy is nonnegligible for a few-mm-thick layer of liquid considered in Refs[15,17]., it mainly affects the stability of the flow [34].) Once the flow in the liquid layer is found, the remaining undetermined fields can be computed from the corresponding transport equations.

The previous numerical simulations [17] were performed for the temperature difference $\Delta T = 6$ K used in the experiments of Li and Yoda [15]. At this relatively high ΔT, in both studies the flow was found to be unsteady for intermediate values of the mean air concentration $\bar{X}_a$. The present study uses two-dimensional numerical simulations at a lower $\Delta T = 2$ K, $\bar{Y}_m = 0.6$ (i.e., 60% methanol and 40% water), and a fixed contact angle of 90 degrees, unless noted otherwise. At this ΔT the flow (cf. Fig. 3) is essentially steady over the entire range of $\bar{X}_a$, so numerical results can be used to both motivate and validate the analytical predictions. At $\bar{X}_a = 0.7$ phase change is suppressed, thermocapillary stresses dominate, and the interfacial flow is in the direction opposite the imposed temperature gradient. Decreasing the concentration of air to $\bar{X}_a = 0.015$ enhances phase change, solutocapillary stresses become dominant, and the direction of the flow reverses.

3.1. Mass transport and concentration profile in the gas phase

Let us start by deriving the analytical solutions for the concentration profiles, following the analysis in Ref. [26]. With a fixed contact angle of 90 degrees, the liquid-gas interface is essentially flat, and we can introduce the rescaled coordinates $\chi = x/d_g$ and $\zeta = z/d_g$, such that the gas phase corresponds to $0 < \zeta < 1$ and $0 < \chi < \Gamma_g$, where $\Gamma_g = L/d_g$ is the aspect ratio of the gas layer. In the present problem, $\Gamma_g \approx 6.5$ is relatively large, and our analytical analysis focuses on the central region of the cavity. Since phase change is small in the central region, the vertical component of the flow there is small ($u_z = O(\Gamma_g^{-1})$), while the horizontal component can be decomposed

$$u_x = \bar{u} + \tilde{u}(\zeta) + O(\Gamma_g^{-1}) \tag{35}$$

into the mean flow $\bar{u}$ and zero-mean recirculation flow $\tilde{u}$. Using this decomposition, the mass transport Eq. (12) in steady state can be solved [26] to leading order in Γ_g^{-1}, yielding

$$X_b = C_{b,0} + C_{b,1}e^{-Pe_{b,m}\chi}[1 + g_b(\zeta)], \tag{36}$$

where

$$g_b(\zeta) = \frac{\bar{u}d_g^2}{\mathfrak{D}_b^2}\int d\zeta' \int_0^{\zeta'} d\zeta''\tilde{u}(\zeta'') + O(\epsilon_b^2), \tag{37}$$

$\epsilon_b = Pe_{b,m}Pe_{b,r}$ is the product of a pair of Peclet numbers, one corresponding to the mean flow

$$Pe_{b,m} = \frac{|\bar{u}|d_g}{\mathfrak{D}_b} \tag{38}$$

and another corresponding to the recirculation flow

$$Pe_{b,r} = \max_\zeta \frac{|\tilde{u}|d_g}{\mathfrak{D}_b}. \tag{39}$$

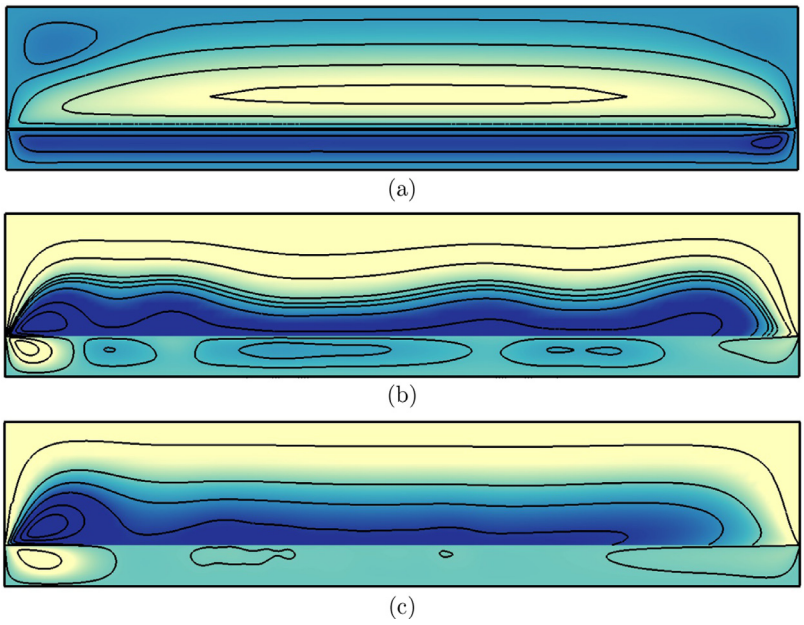

Fig. 3. Numerical solution for the fluid flow with (a) $\bar{X}_a = 0.7$, (b) $\bar{X}_a = 0.1$, (c) $\bar{X}_a = 0.015$. The cold end wall is on the left. Solid lines represent the stream lines of the flow; color corresponds to the values of stream function ψ, where darker (lighter) indicates higher (lower) values of ψ. At $\bar{X}_a = 0.7$, convection rolls in the liquid are all counterclockwise, at $\bar{X}_a = 0.1$, two convection rolls next to both end walls become clockwise, and at $\bar{X}_a = 0.015$, all convection rolls become clockwise. Accordingly, the flow direction along the interface reverses as $\bar{X}_a$ decreases, as shown in Fig. 13.

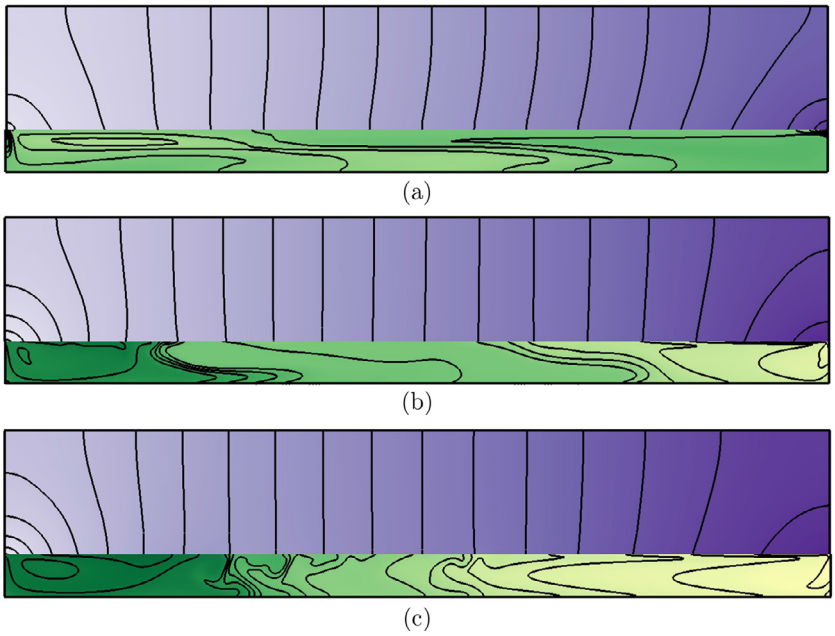

Fig. 4. Numerical solution for the concentration of methanol at (a) $\bar{X}_a = 0.7$, $Y_m = 0.6 \pm 1.89 \times 10^{-4}$, $X_m = 0.26 \pm 0.010$, (b) $\bar{X}_a = 0.1$, $Y_m = 0.6 \pm 1.25 \times 10^{-3}$, $X_m = 0.78 \pm 0.013$, (c) $\bar{X}_a = 0.015$, $Y_m = 0.6 \pm 1.42 \times 10^{-3}$, $X_m = 0.86 \pm 0.003$. Solid lines represent equispaced level sets of the concentration fields (15 in the liquid and 20 in the gas). In both phases, the lighter (darker) color indicates lower (higher) concentration.

The solution (36) depends on both the horizontal coordinate χ and the vertical coordinate ζ, where the ζ-dependence is weak for small ϵ_b, since $g_b(\zeta) = O(\epsilon_b)$. In the limit $\epsilon_b \to 0$, the ζ-dependence disappears:

$$X_b = C_{b,0} + C_{b,1} e^{-Pe_{b,m}\chi}. \tag{40}$$

Indeed, $\epsilon_w \approx \epsilon_m \ll 1$ regardless of the concentration $\bar{X}_a$ of air, as long as ΔT is sufficiently small, so the concentration field should be weakly dependent on the vertical coordinate, and the solution (40) should remain a good approximation even when $Pe_{b,r}$ is not small. This is consistent with the results of our numerical simulations: as Fig. 4 shows, in the central region of the cavity, the variation of the concentration in the vertical direction is negligible compared with that in the horizontal direction.

The constants $C_{b,0}$ and $C_{b,1}$ can be found in explicit analytical form for sufficiently small ΔT. Let the temperature at inner surfaces of the end walls be $T_i^{\pm} = T_0 \pm \Delta T'/2$, where the superscript - (+) refers to the value at $x = 0$ ($x = L$). Eq. (18) implies that the interfacial temperature is essentially equal to the saturation temperature, $T_i \approx T_{s,m} \approx T_{s,w}$, due to the large values of the ratio T_b/T_i (for water and methanol, $T_w = 4.9 \times 10^3$ K and $T_m = 2.8 \times 10^3$ K) and low values of $u_g/u_{t,b}$ [35]. Furthermore, numerical results

show that the variation of Y_b along the interface is very small, so both Y_b and γ_b can be considered fixed at their average values, such that (15) and (17) yield

$$\ln\frac{X_b^{\pm}}{X_b^0} = -T_b\left[\frac{1}{T_0 \pm \Delta T'/2} - \frac{1}{T_0}\right], \tag{41}$$

where X_b^0 is the reference (equilibrium) value of the concentration at $T = T_0$. The variation $(X_b - X_b^0)/X_b^0$ in the vapor concentrations is more pronounced, but still small, so the left-hand-side of (41) can be Taylor-expanded. Since $\Delta T' < \Delta T \ll T_0^2/T_b$, we can also Taylor-expand the right-hand-side. Keeping only the leading-order terms, we find

$$X_b^{\pm} = X_b^0\left[1 \pm \frac{T_b\Delta T'}{2T_0^2}\right]. \tag{42}$$

Finally, substituting these boundary conditions into (40) we find

$$C_{b,0} = X_b^0\left[1 + \frac{T_b\Delta T'}{2T_0^2}\coth\frac{\kappa_b}{2}\right],$$
$$C_{b,1} = -X_b^0\frac{T_b\Delta T'}{T_0^2}\frac{1}{1-e^{-\kappa_b}}, \tag{43}$$

where we have defined $\kappa_b = Pe_{b,m}\Gamma_g$, and

$$\bar{X}_b = X_b^0\left[1 + \frac{T_b\Delta T'}{2T_0^2}\left(\coth\frac{\kappa_b}{2} - \frac{2}{\kappa_b}\right)\right]. \tag{44}$$

3.2. Net heat and mass flux

In order to compare the analytical and numerical results of the concentration profiles in the gas phase quantitatively, we next determine the mean mass flux and the mean gas velocity. The mean (z-averaged) mass flux across the vertical plane at horizontal location x

$$\bar{J}_b(x) = \frac{1}{d_g}\int_x^L J_{i,b}(x')\,dx', \tag{45}$$

can be obtained by integrating the local mass flux $J_{i,b}$ for phase change. Since evaporation (condensation) takes place mainly near the hot (cold) end wall (cf. Fig. 5), the function becomes essentially constant $\bar{J}_b(x) \approx \bar{J}_b^c$ in the central region of the cavity (cf. Fig. 6), where

$$\bar{J}_b^c = \max_x \bar{J}_b(x). \tag{46}$$

We will therefore use the values given by (46) to describe the numerical results and drop the superscript c in the subsequent discussion.

Next, let us estimate the mean mass fluxes $\bar{J}_b$ analytically and consider their dependence on the concentration of air $\bar{X}_a$. For sufficiently low ΔT and highly volatile fluids, the overall heat transport between the end walls is dominated by the latent heat associated with phase change, and the heat flux balance gives

$$\sum_b \bar{J}_b\mathcal{L}_b = \frac{\Delta T}{Z_T}, \tag{47}$$

where Z_T is the total net thermal resistance

$$Z_T = Z_o + Z_d, \tag{48}$$

Z_o is the thermal resistance due to conduction through the liquid layer and the end walls and Z_d is the diffusive resistance of the gas layer [36]. While Z_o can be considered independent of the air concentration $\bar{X}_a$, Z_d is an increasing function of $\bar{X}_a$.

Since heat flows though the walls and the liquid wedges between the wall and the interface "in series," Z_o is a sum of the conduction resistances of the end walls $Z_w = h_s/k_s$ and the conduction resistances of the liquid wedges $Z_l \approx 0.5d_l/k_l$, where

$$Z_o = 2(Z_w + Z_l) \approx 2\frac{h_s}{k_s} + \frac{d_l}{k_l}. \tag{49}$$

The heat flux associated with the mass flux of the two vapors is "in parallel," so that

$$Z_d^{-1} = \sum_b Z_{d,b}^{-1}, \tag{50}$$

where $Z_{d,b}$ is the diffusive resistance associated with component b. Furthermore, the latent heat associated with the phase change of two components is related to their diffusive resistances

$$\frac{\bar{J}_m\mathcal{L}_m}{\bar{J}_w\mathcal{L}_w} = \frac{Z_{d,w}}{Z_{d,m}}. \tag{51}$$

The diffusive resistance for each component $Z_{d,b}$ can be computed from (47) in the limit $\bar{X}_a \to 1$. In this limit, the temperature drop across the end walls can be neglected, so that $\Delta T' = \Delta T$, $Z_o \ll Z_d$, and $Z_T = Z_d$. According to numerical simulations, mass transport is essentially one-dimensional in the central portion of the cavity and, in steady state, the horizontal components of the number flux of each component vapor and air satisfy

$$\bar{j}_m = n_g\mathfrak{D}_m\partial_x X_m - n_g\bar{u}X_m,$$
$$\bar{j}_w = n_g\mathfrak{D}_w\partial_x X_w - n_g\bar{u}X_w,$$
$$0 = n_g\mathfrak{D}_a\partial_x X_a - n_g\bar{u}X_a, \tag{52}$$

where $\bar{j}_b$ is the mean (z-averaged) value of the number flux of the vapor of component b and $\bar{j}_a = 0$ because it is noncondensable.

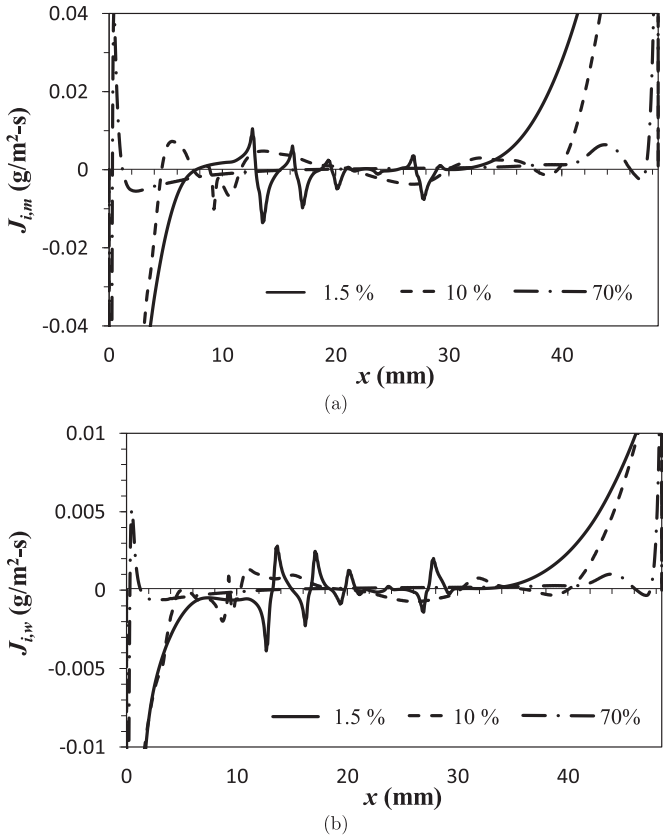

Fig. 5. Mass flux $J_{i,b}$ ($= m_b^1 j_{i,b}$) associated with phase change calculated numerically for (a) methanol and (b) water at three different concentrations of air: $\bar{X}_a = 0.015$ (solid line), $\bar{X}_a = 0.1$ (dashed line) and $\bar{X}_a = 0.7$ (dash dot line). To highlight the variation of the mass flux in the central region of the cavity, the y-axis is truncated in (a) and (b).

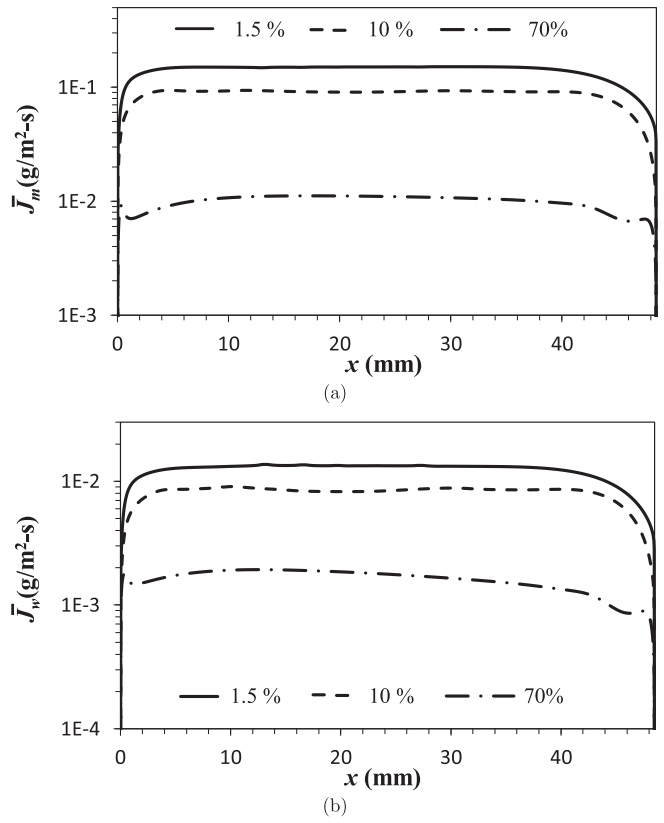

Fig. 6. Mean mass flux $\bar{J}_b$ $(= m_b^1 \bar{j}_b)$ across the vertical cross-section of the cavity computed numerically for (a) methanol and (b) water vapor with three different concentrations of air: $\bar{X}_a = 0.015$ (solid line), $\bar{X}_a = 0.1$ (dashed line) and $\bar{X}_a = 0.7$ (dash dot line).

Summing these equations yields

$$\bar{j}_m + \bar{j}_w = -n_g \bar{u}, \tag{53}$$

where we used the fact that the total diffusive flux vanishes [17]

$$\sum_\iota n_g \mathfrak{D}_\iota \partial_x X_\iota = 0. \tag{54}$$

Solving the system of Eq. (52) together with (53) for $\bar{j}_m$ and $\bar{j}_w$ and integrating the resulting relations from $x = 0$ to $x = L$ yields

$$\bar{j}_m = \frac{n_g}{\bar{X}_a L}\left[\mathfrak{D}_m(1-\bar{X}_w)\Delta X_m + \mathfrak{D}_w \bar{X}_m \Delta X_w\right],$$
$$\bar{j}_w = \frac{n_g}{\bar{X}_a L}\left[\mathfrak{D}_w(1-\bar{X}_m)\Delta X_w + \mathfrak{D}_m \bar{X}_w \Delta X_m\right], \tag{55}$$

where, according to (42),

$$\Delta X_b = X_b|_{x=L} - X_b|_{x=0} = X_b^0 \frac{T_b \Delta T}{T_0^2} \ll \bar{X}_b. \tag{56}$$

From (47), (50), (55), and (56) we find

$$Z_{d,m} = \frac{\bar{X}_a T_0^3 L}{p_g \bar{X}_m T_m \left[\mathfrak{D}_m(1-\bar{X}_w)T_m + \mathfrak{D}_w \bar{X}_w T_w\right]},$$
$$Z_{d,w} = \frac{\bar{X}_a T_0^3 L}{p_g \bar{X}_w T_w \left[\mathfrak{D}_w(1-\bar{X}_m)T_w + \mathfrak{D}_m \bar{X}_m T_m\right]}. \tag{57}$$

Note that, in the limit $\bar{X}_w \to 0$ $(\bar{X}_m \to 0)$, the diffusive resistance $Z_{d,m}$ $(Z_{d,\,w})$ reduces to the expression $Z_d = L/k_c$, where k_c is the effective condensation thermal conductivity derived for a binary (vapor/air) mixture by Peterson et al. [37].

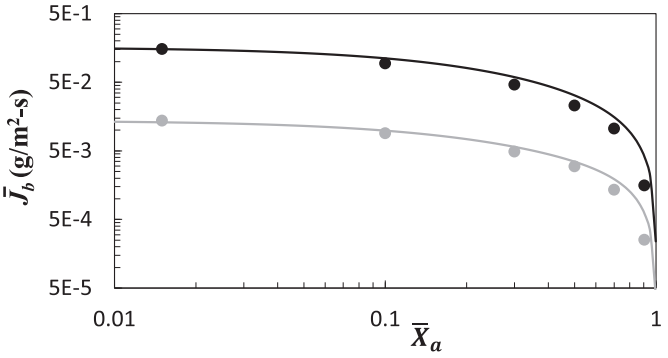

Fig. 7. The characteristic mass fluxes $\bar{J}_b$ $(= m_b^1 \bar{j}_b)$ in the gas phase. The results for methanol (water) are shown in black (grey). Solid line represents the analytical estimate based on (58), symbols – the numerical results obtained using (46).

Finally, solving (47) and (51) we find

$$\bar{J}_b = \left[1 + Z_o \sum_b Z_{d,b}^{-1}\right]^{-1} \frac{\Delta T}{\mathcal{L}_b}. \tag{58}$$

Fig. 7 shows that the analytical and numerical results are in reasonable agreement, suggesting that the one-dimensional description of transport in the gas phase is reasonably accurate. An increase in $\bar{X}_a$ leads to an increase in the diffusive resistance for both component vapors and, correspondingly, a decrease in both fluxes. The minor discrepancy between the numerical and analytical results is likely due to the contribution of heat conduction and advection in the liquid layer that have been ignored in our analysis. These contributions are negligible for low $\bar{X}_a$, but would become progressively more important at higher $\bar{X}_a$, when phase change is suppressed, and our estimates of $\bar{j}_b$ are expected to overestimate the numerical results, consistent with Fig. 7. In practical applications (*e.g.*, for heat pipes) the liquid layer will be substantially thinner, so convective heat flux would be negligible and the prediction of our simplified transport model would be even more accurate.

Once the mean vapor fluxes and the mean flow velocity have been determined from (47) and (53), we can finally compare the analytical prediction (40) for the concentration profiles with the numerical results. As Fig. 8 shows, we find good agreement (minor deviations will be discussed in the next Section). In general, the concentrations of all components in the ternary gas mixture vary exponentially with x, which is consistent with the findings for simple fluids with binary (vapor/air) gas mixtures [25]. The exponential concentration profiles become approximately linear when $Pe_{b,m} \ll \Gamma_g^{-1}$. This limit corresponds to low values of the mean flow velocity $\bar{u}$ and hence low values of ΔT and/or high values of $\bar{X}_a$. In particular, at $\Delta T = 2$ K, the concentration profiles are nearly linear for all $\bar{X}_a$.

3.3. Interfacial temperature and concentration profiles

As we argued in the previous section, the concentration fields are determined, to leading order, by the net mass flux of the vapors, which is determined by the temperature gradient or, more precisely, by the temperature difference between the end walls, but not the concentration gradient. However, the concentration fields in the gas phase determine both the temperature and liquid concentration at the interface via (17) and (15). With the help of (17) we can write

$$\frac{p_b}{p_b^0} = \frac{X_b \gamma_b^0 Y_b^0}{X_b^0 \gamma_b Y_b}, \tag{59}$$

where the superscript 0 denotes the reference values corresponding to the global thermodynamic equilibrium at $T = T_0$. We can

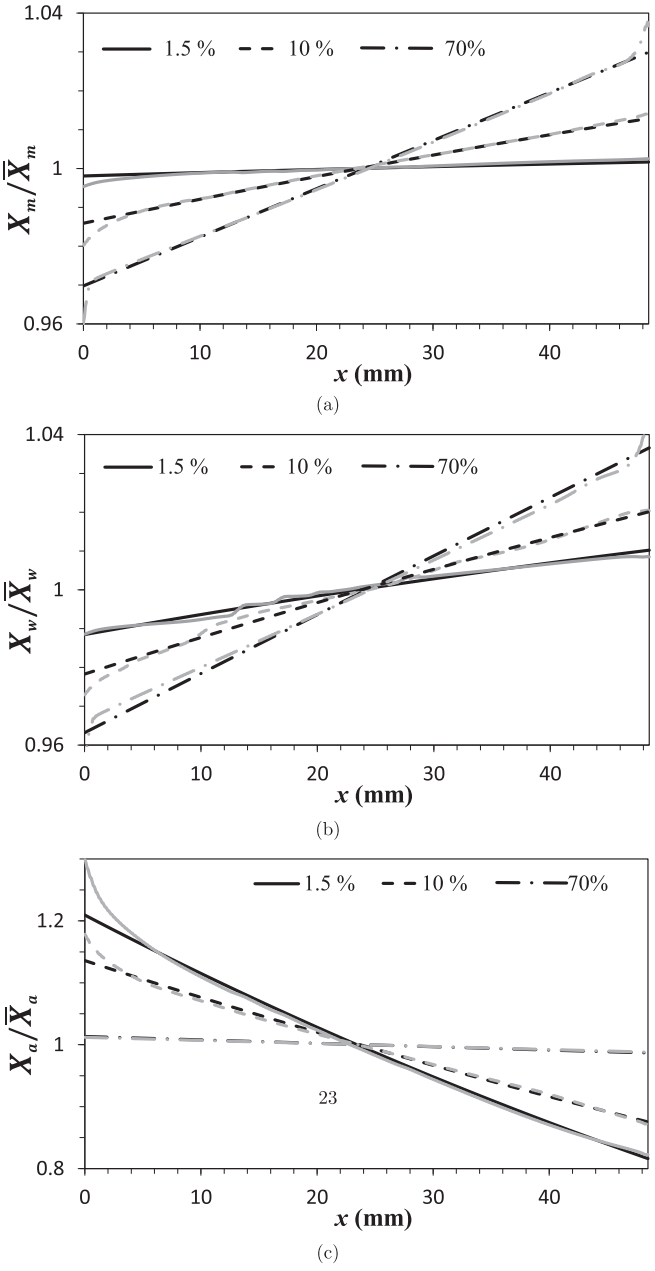

Fig. 8. Normalized concentration profiles in the gas phase for methanol (a), water (b), and air (c) for different $\bar{X}_a$. Numerical and analytical results are represented by gray and black lines, respectively. Numerical results correspond to the horizontal midplane of the gas layer. To highlight the variation in the central region of the cavity, the y-axis is truncated in (a) and (b).

replace the reference values of all the concentrations with the mean values, $Y_b^0 = \bar{Y}_b$, $\gamma_b^0 = \bar{\gamma}_b = \gamma_b(\bar{Y}_b)$, and $X_b^0 = \bar{X}_b$. One the other hand, the phase equilibrium condition (15) requires

$$\frac{p_b}{p_b^0} = e^{T_b/\theta}, \tag{60}$$

where we have defined a new variable θ according to

$$\frac{1}{\theta} = \frac{1}{T_0} - \frac{1}{T_i} \approx \frac{\delta T_i}{T_0^2}, \tag{61}$$

where $\delta T_i = T_i - T_0$. Equating the right-hand-sides of (59) and (60), we find

$$Y_b = \frac{X_b \bar{\gamma}_b \bar{Y}_b}{\gamma_b \bar{X}_b} e^{-T_b/\theta}. \tag{62}$$

Since Y_b is very close to $\bar{Y}_b$, the dependence of the activity coefficient on the concentration is described with very good accuracy by a linear relationship

$$\gamma_b(Y_b) = \bar{\gamma}_b + \gamma_b'(Y_b - \bar{Y}_b), \tag{63}$$

where $\gamma_b' = \partial\gamma_b/\partial Y_b$ at $Y_b = \bar{Y}_b$. The liquid is a binary mixture, so $Y_m + Y_w = \bar{Y}_m + \bar{Y}_w = 1$, which yields a transcendental equation for θ

$$\sum_b h_b\left[1 - a_b e^{-T_b/\theta}\right] = 0, \tag{64}$$

where the sum is over $b = m$, w and

$$h_b = \frac{\bar{Y}_b}{1 + \gamma_b'\bar{Y}_b}, \qquad a_b = \frac{X_b}{\bar{X}_b}. \tag{65}$$

This equation can be solved approximately for small deviations of the interfacial temperature from T_0, i.e., for $|\theta| \gg \max(T_m, T_w)$ by Taylor-expanding both exponential terms. Indeed it is easy to see that $|\theta| \geq O(T_0^2/\Delta T) = O(10^4\ \mathrm{K})$ for ΔT as large as 10 K. The actual temperature variation along the interface is typically a fraction of ΔT, leading to an even higher $|\theta|$ (e.g., $|\theta| \sim O(10^5\ \mathrm{K})$ at $\Delta T = 2$ K), so that reasonably accurate results can be obtained in analytic form by truncating the Taylor series at linear terms, which yields

$$\frac{1}{\theta} = \frac{\sum_b h_b(a_b - 1)}{\sum_b h_b a_b T_b}. \tag{66}$$

The corresponding interfacial temperature can now be found from (61) and the interfacial concentrations of water and methanol in the liquid phase from (62).

The analytical predictions for the interfacial temperature are in reasonable agreement with the numerical results in the central region (cf. Fig. 9). Based on (15), the temperature gradient is related to the vapor pressure gradient and hence the gas concentration gradient, so the nearly linear concentration profiles at $\Delta T = 2$ K should imply nearly linear interfacial temperature profiles for all $\bar{X}_a$. Note that this is *not* a reflection of the thermal boundary conditions at the top/bottom wall, but rather a result of mass transport in the gas phase.

The theoretical interfacial concentration profiles predict the overall variation correctly, but exhibit noticeable local deviations from the concentration profiles found in the numerical simulations, as Fig. 10 illustrates. This is due to the insufficient accuracy in our description of the concentration fields X_b in the gas phase. While the analytical and numerical results of X_b appear to agree quite well (cf. Fig. 8), even relatively small discrepancies (they are most

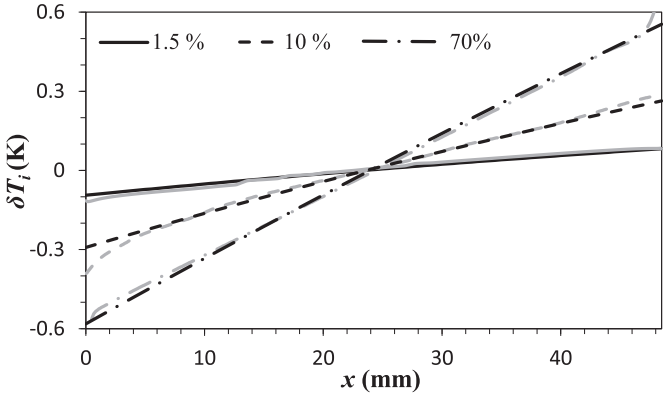

Fig. 9. Interfacial temperature for different $\bar{X}_a$. The variation $\delta T_i = T_i - T_0$ about the mean is plotted. Numerical and analytical results are represented by gray and black lines, respectively. To highlight the variation of the interfacial temperatude in the central region of the cavity, the y-axis is truncated.

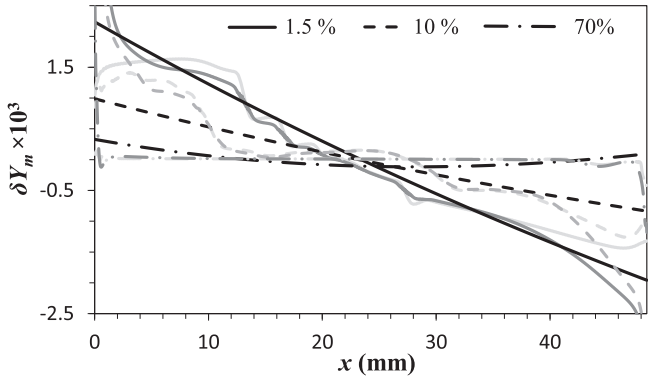

Fig. 10. The interfacial concentration of methanol in the liquid for different $\bar{X}_a$. The variation $\delta Y_m = Y_m - \bar{Y}_m$ about the mean is plotted. Black lines represent the analytical estimate (62) based on the analytical solution for X_m and T_i, dark gray lines – the numerical results, and light gray lines – the analytical estimate (62) based on the numerical results for X_m and T_i. To highlight the variation of the interfacial concentration in the central region of the cavity, the y-axis is truncated.

noticeable for X_w) are greatly amplified because of the exponential dependence of Y_b on the ratio T_b/θ in (62). To illustrate this, we computed the interfacial profile of Y_m by substituting numerical, rather than analytical, results for the concentration fields X_m and X_w into Eq. (62). As Fig. 10 shows, the resulting estimate accurately reproduces even the fine details of the numerical solution for Y_m in the central region of the cavity, confirming that it is indeed the accuracy of the estimate (40) that is the culprit. (The remaining discrepancy near the end walls is mainly due to the difference between T_i and $T_{s,b}$.)

The origin of the local deviation of the analytical solution (40) from the numerical one at the two lower values of $\bar{X}_a$ can be easily identified by inspecting the flow field (cf. Fig. 3), methanol concentration in the liquid (cf. Fig. 4), and the phase change flux at the interface (cf. Fig. 5). The flow at the intermediate value of $\bar{X}_a$ shown in Fig. 11 features several convection rolls in the liquid layer. The composition of the liquid layer is controlled by advection, which dominates over diffusion due to a very low value of D_l (and a correspondingly large mass Péclet number). Convection rolls effectively convert the horizontal gradient of Y_m driving the mean flow into the vertical gradient.

The analysis presented in Section 3.1 completely ignored phase change in the central region of the cavity. However, even though it is far less intense than near the end walls, phase change also occurs in the central region (cf. Fig. 5). The vertical mass flux in the liquid layer causes evaporation of methanol at the left edge of each counter-rotating convection roll and condensation at the right edge, as demonstrated by the phase change flux $J_{i,m}$. This phase change acts as a perturbation on the flow field in the gas layer (the clearly visible modulation of the stream lines in the top panel of Fig. 11). As the relation (37) illustrates, a perturbation in the flow field generates a corresponding perturbation in the concentration fields X_b described by (36) and it is this perturbation that is responsible for the deviation of the predicted composition of the liquid at the interface from the actual composition that is observed (bottom panel of Fig. 11). The deviation of the predicted interfacial concentration profile at $\bar{X}_a = 0.7$ is also due to the nonnegligible phase change in the central region of the interface (cf. Fig. 5), even though in this case there is no convection pattern.

The spatial variation in the temperature and composition of the liquid at the interface generates thermocapillary and solutocapillary stresses, respectively. These stresses will be discussed in more detail next, but we conclude this Section by noting that our analysis points to the perturbation in Y_m, shown in the bottom panel of Fig. 11, causing both the phase change in the central region of

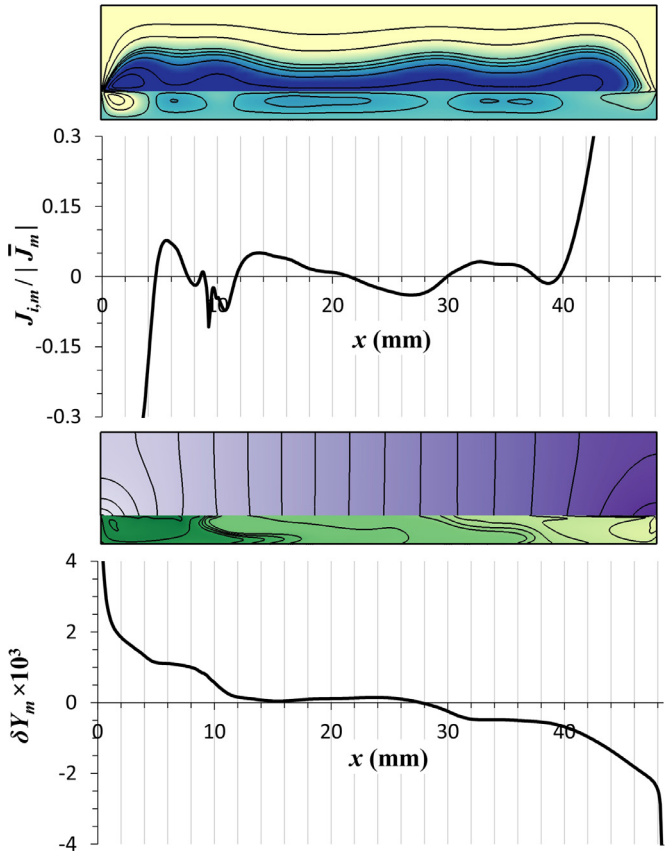

Fig. 11. Numerical solution for $\bar{X}_a = 0.1$, $\bar{Y}_m = 0.6$. The panels shows (from top to bottom) the flow field, the normalized mass flux associated with the condensation/evaporation of methanol, the concentration of methanol in both phases, and the variation δY_m of the methanol concentration in the liquid about the mean.

the cavity and the modulation of solutocapillary stresses that give rise to the convection rolls. The detailed stability analysis of this problem that couples the perturbations in the flow and composition of both layers is outside the scope of this paper, although the mechanism of the instability appears to be clear.

3.4. The Marangoni stresses and interfacial flow

With the solutions for the interfacial temperature and concentration profiles in hand, we can immediately determine the thermocapillary and solutocapillary stresses. The net surface stress $\partial_x \sigma = \Sigma_S + \Sigma_T$ is the sum of the solutocapillary stress

$$\Sigma_S = F_S \partial_x Y_m \tag{67}$$

and thermocapillary stress

$$\Sigma_T = F_T \partial_x T_i, \tag{68}$$

where, according to (31), we have defined

$$F_S = f'(Y_m)(\sigma_m - \sigma_w) < 0, \tag{69}$$

and

$$F_T = -f(Y_m)\sigma_m' - (1 - f(Y_m))\sigma_w' < 0. \tag{70}$$

Taking the derivative of (62) we obtain

$$\partial_x Y_b \approx \frac{\bar{Y}_b}{s_b}\left[\frac{\partial_x X_b}{X_b} - \frac{T_b \partial_x T_i}{T_i^2}\right], \tag{71}$$

where

$$s_b = 1 + \frac{\gamma_b'}{\bar{\gamma}_b}\bar{Y}_b. \tag{72}$$

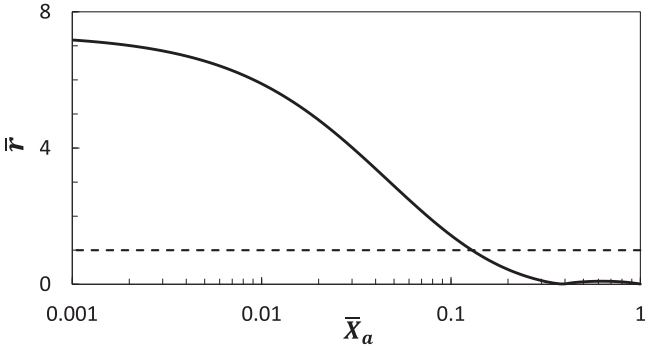

Fig. 12. The ratio of solutocapillary and thermocapillary stresses for different $\bar{X}_a$ evaluated using (73) with mean values of $\partial_x X_m$ and $\partial_x T_i$. The dashed line represents the exact balance between the mean solutocapillary and thermocapillary stresses, $\bar{r} = 1$.

Therefore the ratio of solutocapillary and thermocapillary stresses can be estimated as

$$r \equiv -\frac{\Sigma_S}{\Sigma_T} \approx \frac{F_S \bar{Y}_m}{s_m F_T \bar{X}_m}\left[\frac{X_m T_m}{T_i^2} - \frac{\partial_x X_m}{\partial_x T_i}\right], \tag{73}$$

where the minus sign reflects their (typically) opposite direction. When both concentration and temperature profiles are nearly linear, the derivatives $\partial_x X_m$ and $\partial_x T_i$ are nearly constant, so r does not vary significantly along the interface. At lower air concentrations, however, $\partial_x Y_m$ can vary considerably and can even change sign, as shown in Fig. 11. Hence it will be convenient to quantify the relative strength of the two stresses using the ratio of their mean values, $\bar{r}$, shown in Fig. 12, which corresponds to the mean values of $\partial_x X_m$ and $\partial_x T_i$ in (73).

In the limit $\bar{X}_a \to 1$ (e.g., at ambient conditions), the differential phase change responsible for generating solutocapillary stresses is greatly suppressed, such that $Y_m \to \bar{Y}_m$ and consequently $\Sigma_S \to 0$, which means that the flow is controlled entirely by thermocapillary stresses. The numerical results (cf. Fig. 13) show that the flow at the interface is indeed towards the cold end ($u_i < 0$) along the entire interface, with a nearly constant velocity in the central region of the cavity, which is consistent with a nearly constant temperature gradient.

As $\bar{X}_a$ decreases, the ratio $\bar{r}$ increases, reflecting the increase of solutocapillarity stresses associated with increased differential phase change. The mean soluto- and thermocapillary stresses become comparable, $\bar{r} = 1$, around $\bar{X}_a = 0.1$, at which point we find the flow reversing its direction at multiple locations along the interface (cf. Fig. 13), depending on whether the local value of r is above or below unity. This is consistent with the pattern of convection rolls shown in Fig. 11. As the concentration of air is reduced even further, $\bar{r}$ increases above unity (e.g., $\bar{r} \approx 5$ at $\bar{X}_a = 0.015$), reflecting the dominant role of solutocapillary stresses. Correspondingly, the flow towards the hot end wall along almost the entire interface is found.

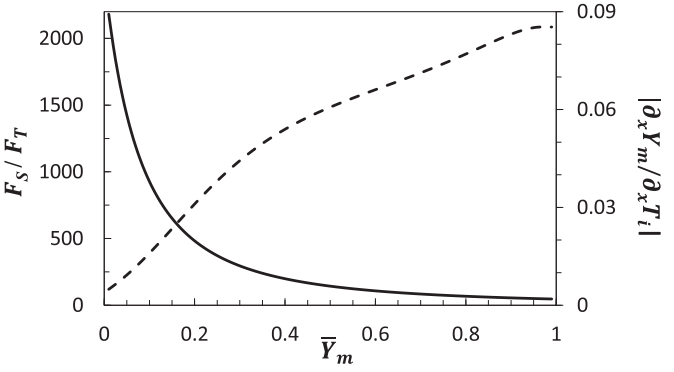

Fig. 14. The ratio of the coefficients F_S/F_T (solid line) and the gradients $|\partial_x Y_m/\partial_x T_i|$ (dashed line) at $\bar{X}_a = 0$.

The limit $\bar{X}_a \to 0$ is the most interesting from the perspective of evaporative cooling, where solutocapillarity can ameliorate the adverse effect of thermocapillary stresses leading to dry-out. In this limit $X_m + X_w = 1$, so that

$$\partial_x X_m = -\partial_x X_w, \tag{74}$$

which allows us to make further progress. Combining the relation (71) for both water and methanol with (74), we find

$$r = \frac{F_S}{F_T}\frac{\bar{X}_m T_m + \bar{X}_w T_w}{T_0^2}\left(\frac{s_m \bar{X}_m}{\bar{Y}_m} - \frac{s_w \bar{X}_w}{\bar{Y}_w}\right)^{-1}, \tag{75}$$

since in this limit X_m and X_w almost coincide with their average values. This result predicts that the ratio of solutocapillary and thermocapillary stresses becomes constant in the limit $\bar{X}_a \to 0$, so the flow should become strictly unidirectional, just like in the opposite limit $\bar{X}_a \to 1$, but with the opposite direction.

As Fig. 14 illustrates, for water-methanol mixture, the ratio F_S/F_T is a monotonically decreasing function of $\bar{Y}_m$, while the ratio $|\partial_x \bar{Y}_m/\partial_x \bar{T}_i|$ is a monotonically increasing function, so predicting the trend for r is not straightforward. Evaluating the product of these two ratios shows that r has a peak value around 15 at $\bar{Y}_m \approx 0.15$ (cf. Fig. 15), which represents the optimal composition of the liquid that maximizes the favorable solutocapillary stresses. Indeed, the numerical simulations in the same geometry for $\Delta T = 6$ K and $\bar{X}_a = 0.015$ reported in Ref. [17] illustrate the same nonmonotonic

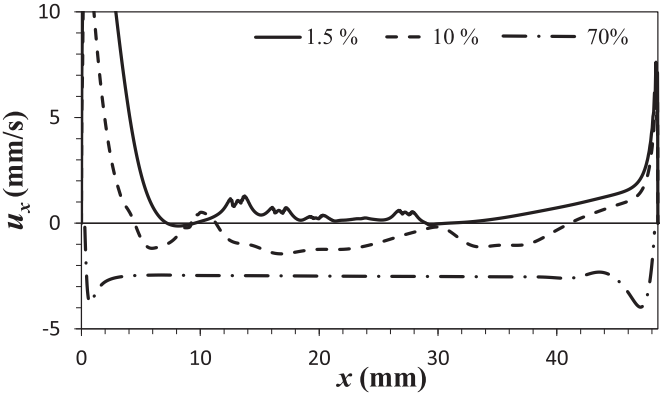

Fig. 13. Interfacial velocity (numerical) for different $\bar{X}_a$. To highlight the variation of interfacial velocity in the central region of the cavity, the y-axis is truncated.

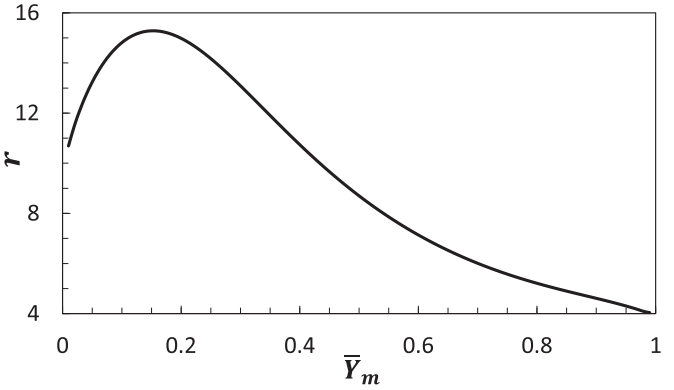

Fig. 15. Dependence of the ratio of the solutocapillary and thermocapillary stresses on $\bar{Y}_m$ at $\bar{X}_a = 0$.

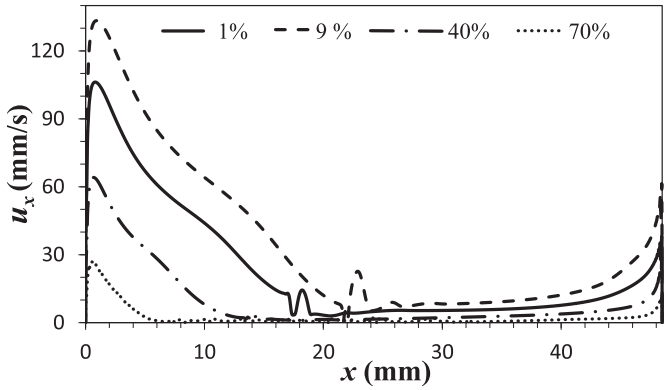

Fig. 16. Dependence of the interfacial velocity (numerical) on $\bar{Y}_m$ at $\bar{X}_a = 0.015$ and $\Delta T = 6$ K.

dependence on the composition of the liquid. As Fig. 16 shows, the interfacial velocity is the largest at relatively small but nonzero concentrations of methanol (e.g., $\bar{Y}_m = 0.09$) and decreases at both lower concentrations (e.g., $\bar{Y}_m = 0.01$) and higher concentrations (e.g., $\bar{Y}_m = 0.4$ and $\bar{Y}_m = 0.7$). While these numerical velocity profiles are only available for a discrete set of $\bar{Y}_m$, they are completely consistent with the theoretical prediction based on our simplified analysis.

As discussed in Section 3.3, although the analytical solution for the interfacial concentration profile that ignores phase change in the central region of the cavity does not give an accurate local prediction for solutocapillary stresses in the presence of a short wave length convection pattern, the mean ratio $\bar{r}$ correctly predicts the dominant contribution to the Marangoni stress and hence the direction of the flow along the interface for different $\bar{X}_a$. The variation of r about the mean value $\bar{r}$ is due to convection in the liquid layer, which should be suppressed for thin liquid films, since the Marangoni number scales with the square of the layer thickness d_l and the Rayleigh number scales as d_l^4 [28]. Hence, for sufficiently thin films, we should expect $r \approx \bar{r}$ and the interfacial flow velocity to be nearly uniform for all $\bar{X}_a$.

4. Conclusions

By analyzing the comprehensive two-sided transport model for a volatile binary liquid driven by an externally applied temperature gradient [17] and its numerical solutions we demonstrated that, despite its complexity, the problem can be described analytically in certain useful limits. Not surprisingly, the analytical description approximates the numerical results well when the flow is relatively simple, with no spatially or temporally complicated convection pattern. In the presence of convection rolls, our analysis can predict the mean flow and the mean gradients of various quantities with reasonable accuracy, but not the spatial/temporal modulation describing the convective pattern.

In modeling two-phase flows, it is a common practice to either ignore the transport in the gas phase or describe it through effective boundary conditions at the free surface. For volatile binary liquids, this approach fails in a rather spectacular manner. Our analysis shows that, for fluid layers with sufficiently high aspect ratio, the transport equations for mass, heat, and momentum can be solved sequentially, starting with the bulk concentration fields in the gas phase. These concentration fields determine the temperature and composition of the liquid layer at the interface and, consequently, the Marangoni (thermocapillary and solutocapillary) stresses. The Marangoni stresses, in turn, control the flow in the liquid layer, which eventually determines the bulk temperature and concentration field in the liquid and the flow in the gas layer, yielding a complete solution of the problem. This result generalizes a similar conclusion for two-phase flows of volatile simple fluids [25,26].

We derived explicit analytical expressions for the mean solutocapillary and thermocapillary stresses which correctly predict when the direction of the interfacial flow reverses. In particular, when the gas is predominantly air ($\bar{X}_a \to 1$), such as under ambient conditions, as phase change is greatly suppressed, solutocapillary stresses were found to vanish, and thermocapillary stresses drive the interfacial flow in the direction opposite to the temperature gradient. In the opposite limit, when the air is removed almost completely ($\bar{X}_a \to 0$), phase change is enhanced and solutocapillary stresses dominate, driving the flow in the direction of the temperature gradient. Interestingly, the thermocapillary stresses do not vanish in this limit for volatile binary liquids, unlike volatile simple liquids for which thermocapillary stresses completely disappear [25,35].

Our results also provide useful guidelines for choosing the composition of binary coolants and the optimal operating conditions for thermal management applications. In particular, the concentration of air in a sealed cavity needs to be below 10% or so for the solutocapillarity to balance the adverse effect of thermocapillary stresses. Solutocapillary effect plays a beneficial role in general, helping drive the liquid coolant towards the hot spots. Due to the monotonic dependence of r on $\bar{X}_a$ (below $\bar{X}_a \lesssim 0.3$), it is beneficial to reduce the air concentration as much as possible. The optimal composition of the binary coolant, on the other hand, corresponds to a small, but finite value of the concentration of the more volatile component, e.g., $\bar{Y}_m \approx 0.15$ for a water-methanol mixture.

Author Declaration

We wish to confirm that there are no known conflicts of interest associated with this publication and there has been no significant financial support for this work that could have influenced its outcome. We confirm that the manuscript has been read and approved by all named authors and that there are no other persons who satisfied the criteria for authorship but are not listed. We further confirm that the order of authors listed in the manuscript has been approved by all of us. We confirm that we have given due consideration to the protection of intellectual property associated with this work and that there are no impediments to publication, including the timing of publication, with respect to intellectual property. In so doing we confirm that we have followed the regulations of our institutions concerning intellectual property. We understand that the Corresponding Author is the sole contact for the Editorial process (including Editorial Manager and direct communications with the office). He is responsible for communicating with the other authors about progress, submissions of revisions and final approval of proofs. We confirm that we have provided a current, correct email address which is accessible by the Corresponding Author and which has been configured to accept email from tongran@gatech.edu.

CRediT authorship contribution statement

Tongran Qin: Conceptualization, Methodology, Software, Formal analysis, Investigation, Data curation, Visualization, Writing - original draft, Writing - review & editing. **Roman O. Grigoriev:** Conceptualization, Methodology, Formal analysis, Investigation, Writing - review & editing, Supervision, Project administration, Funding acquisition.

Acknowledgments

This work was supported by the National Science Foundation under Grant No. CMMI-1511470.

References

[1] Y. Abe, Self-rewetting fluids, Ann. N. Y. Acad. Sci. 1077 (1) (2006) 650–667.
[2] R. Vochten, G. Petre, Study of the heat of reversible adsorption at the air-solution interface. ii. experimental determination of the heat of reversible adsorption of some alcohols, J. Colloid Interface Sci. 42 (2) (1973) 320–327.
[3] N. di Francescantonio, R. Savino, Y. Abe, New alcohol solutions for heat pipes: Marangoni effect and heat transfer enhancement, Int. J. Heat Mass Transf. 51 (2008) 6199–6207.
[4] A. Cecere, R. Paola, R. Savino, Y. Abe, L. Carotenuto, S. Vaerenbergh, Observation of Marangoni flow in ordinary and self-rewetting fluids using optical diagnostic systems, Eur. Phys. J. Spec. Top. 192 (2011) 109–120.
[5] R. Savino, D.D. Cristofaro, A. Cecere, Flow visualization and analysis of self-rewetting fluids in a model heat pipe, Int. J. Heat Mass Transf. 115 (2017) 581–591.
[6] A. Cecere, D.D. Cristofaro, R. Savino, G. Boveri, M. Raimondo, F. Veronesi, F. Oukara, R. Rioboo, Visualization of liquid distribution and dry-out in a single-channel heat pipes with different wettability, Exp. Therm. Fluid Sci. 96 (2018) 234–242.
[7] R. Savino, A. Cecere, S. Vaerenbergh, Y. Abe, G. Pizzirusso, W. Tzevelecos, M. Mojahed, Q. Galand, Some experimental progresses in the study of self-rewetting fluids for the selene experiment to be carried in the thermal platform 1 hardware, Acta Astronaut. 89 (2013) 179–188.
[8] T.T. Nguyen, A. Kundan, P.C. Wayner, J.L. Plawsky, D.F. Chao, R.J. Sicker, The effect of an ideal fluid mixture on the evaporator performance of a heat pipe in microgravity, Int. J. Heat Mass Transf. 95 (2016) 765–772.
[9] A. Cecere, G. Di Martino, S. Mungiguerra, Experimental investigation of capillary-driven two-phase flow in water/butanol under reduced gravity conditions, Microgravity Sci. Technol. 131 (2019) 425–434.
[10] K. Cheng, C. Park, Surface tension of dilute alcohol-aqueous binary fluids: n-butanol/water, n-pentanol/water, and n-hexanol/water solutions, Heat Mass Transf. 53 (2017) 22552263.
[11] M. Kuramae, M. Suzuki, Two-component heat pipes utilizing the Marangoni effect, J. Chem. Eng. Jpn. 26 (2) (1993) 230–231.
[12] D.M. Pratt, K.D. Kihm, Binary fluid mixture and thermocapillary effects on the wetting characteristics of a heated curved meniscus, J. Heat Transf. 125 (5) (2003) 867–874.
[13] K.M. Armijo, V.P. Carey, An experimental study of heat pipe performance using binary mixture fluids that exhibit strong concentration Marangoni effects, J. Therm. Sci. Eng. Appl. 3 (3) (2011) 31003.
[14] K.M. Armijo, V.P. Carey, An analytical and experimental study of heat pipe performance with a working fluid exhibiting strong concentration marangoni effects, Int. J. Heat Mass Transf. 64 (2013) 70–78.
[15] Y. Li, M. Yoda, An experimental study of buoyancy-Marangoni convection in confined and volatile binary fluids, Int. J. Heat Mass Transf. 102 (2016) 369–380.
[16] W. Minkowycz, E. Sparrow, Condensation heat transfer in the presence of noncondensables, interfacial resistance, superheating, variable properties, and diffusion, Int. J. Heat Mass Transf. 9 (1966) 1125.
[17] T. Qin, R.O. Grigoriev, A numerical study of buoyancy-Marangoni convection of volatile binary fluids in confined geometries, Int. J. Heat Mass Transf. 127 (2018) 308–320.
[18] T. Qin, R.O. Grigoriev, Convection, evaporation, and condensation of simple and binary fluids in confined geometries, in: Proc. of the 3rd Micro/Nanoscale Heat & Mass Transfer International Conference, 2012, pp. MNHMT2012–75266.
[19] J. Kern, P. Stephan, Theoretical model for nucleate boiling heat and mass transfer of binary mixtures, J. Heat Transf. 125 (2003) 1106–1115.
[20] S. Karpitschka, F. Liebig, H. Riegler, Marangoni contraction of evaporating sessile droplets of binary mixtures, Langmuir 33 (2017) 4682–4687.
[21] S. Zhou, L. Zhou, X. Du, Y. Yang, Heat transfer characteristics of evaporating thin liquid film in closed microcavity for self-rewetting binary fluid, Int. J. Heat Mass Transf. 108 (2017) 136–145.
[22] J.-J. Yu, Y.-R. Li, C.-M. Wu, J.-C. Chen, Three-dimensional thermocapillary-buoyancy flow of a binary mixture with Soret effect in a shallow annular pool, Int. J. Heat Mass Transf. 90 (2015) 1071–1081.
[23] J.-J. Yu, Y.-R. Li, J.-C. Chen, Y. Zhang, C.-M. Wu, Thermal-solutal capillary-buoyancy flow of a low Prandtl number binary mixture with various capillary ratios in an annular pool, Int. J. Heat Mass Transf. 113 (2017) 40–52.
[24] J.-J. Yu, C.-Y. Tang, Y.-R. Li, T. Qin, Numerical simulation study on the pure solutocapillary flow of a binary mixture with various solutal coefficients of surface tension in an annular pool, Int. Commun. Heat Mass Transf. 108 (2019) 104342.
[25] T. Qin, R.O. Grigoriev, The effect of noncondensables on buoyancy-thermocapillary convection of volatile fluids in confined geometries, Int. J. Heat Mass Transf. 90 (2015) 678–688.
[26] T. Qin, R.O. Grigoriev, Free-surface flow of confined volatile simple fluids driven by a horizontal temperature gradient: from a comprehensive numerical model to a simplified analytical description, Int. J. Heat Mass Transf. 147 (2020) 118934.
[27] Y. Li, R.O. Grigoriev, M. Yoda, Experimental study of the effect of noncondensables on buoyancy-thermocapillary convection in a volatile low-viscosity silicone oil, Phys. Fluids 26 (2014) 122112.
[28] T. Qin, Z. Tuković, R.O. Grigoriev, Buoyancy-thermocapillary convection of volatile fluids under atmospheric conditions, Int. J. Heat Mass Transf. 75 (2014) 284–301.
[29] T. Qin, Buoyancy-Thermocapillary Convection of Volatile Fluids in Confined and Sealed Geometries, Springer Theses, Springer International Publishing, 2017.
[30] R. Taylor, R. Krishna, Multicomponent Mass Transfer, vol. 2, John Wiley & Sons, 1993.
[31] J.L. Plawsky, M. Ojha, A. Chatterjee, P.C. Wayner, Review of the effects of surface topography, surface chemistry, and fluid physics on evaporation at the contact line, Chem. Eng. Commun. 196 (5) (2008) 658–696.
[32] R.W. Schrage, A Theoretical Study of Interface Mass Transf., Columbia University Press, New York, 1953.
[33] G. Vazquez, E. Alvarez, J.M. Navaza, Surface tension of alcohol water+ water from 20 to 50. degree. C, J. Chem. Eng. Data 40 (1995) 611–614.
[34] R.O. Grigoriev, T. Qin, The effect of phase change on stability of convective flow in a layer of volatile liquid driven by a horizontal temperature gradient, J. Fluid Mech. 838 (2018) 248–283.
[35] T. Qin, Z. Tuković, R.O. Grigoriev, Buoyancy-thermocapillary convection of volatile fluids under their vapors, Int. J. Heat Mass Transf. 80 (2015) 38–49.
[36] J. Liu, R.O. Grigoriev, Analytical solution for filmwise condensation in confined high-aspect ratio geometry, Int. J. Heat Mass Transf. 133 (2019) 561–571.
[37] P.F. Peterson, V.E. Schrock, T. Kageyama, Diffusion layer theory for turbulent vapor condensation with noncondensable gases, J. Heat Transf. 115 (1993) 998–1003.